scientific reports

Check for updates

OPEN

A facile novel synthesis of $AgCuO_2$ delafossite nanoparticles and evaluation of their antimicrobial activity

Ebtesam E. Ateia, M. M. Arman & Amira T. Mohamed✉

Bi-functional nano-oxides are of growing interest to address environmental issues. In the present study, the structural and magnetic data are presented together with the antimicrobial activities (AMA). For the first time, silver delafossite oxide ($AgCuO_2$) is successfully fabricated using a simple, low-cost technique to target antibiotic photodegradation and inactivation of model waterborne pathogens. It is prepared with an equimolar initial Ag^+:Cu^+ concentration ratio. The structure, morphology, and magnetic properties are studied by different characterization techniques. The size and shape of $AgCuO_2$ NPs, in addition to their structural polytypes of 2H (hexagonal) or 3R (rhombohedral), are dependent on the preparation conditions. The existence of Cu, Ag, and O in the synthesized delafossite $AgCuO_2$ NPs with no evidence of any impurity is ratified by the XPS spectrum. AFM measurements are taken to characterize the surface morphologies of $AgCuO_2$. The distributed spiks are evaluated by roughness kurtosis (Rku). The roughness kurtosis has a value of 2.65 (< 3), indicating that the prepared sample is classified as bumpy. The prepared sample has 13.0, 10.0, 14.0, and 14.0 mm Inhibition Zone Diameter (IZD) antimicrobial activity against gram-positive *Bacillus subtilis* (*B. subtilis*), *Bacillus cereus* (*B. cereus*), *Enterococcus faecalis* (*E. faecalis*), and *Staphylococcus aureus* (*S. aureus*), respectively. The IZD for gram-negative *Escherichia coli* (*E. coli*), *Neisseria Gonorrhoeae* (*N. Gonorrhoeae*), *Pseudomonas aeruginosa* (*P. aeruginosa*), and *Salmonella typhimrium* (*S. typhimrium*) were found to be 12.0, 13.0, 14.0, and 13.0 mm, respectively. Therefore, the $AgCuO_2$ NPs reveal excellent antimicrobial efficiency, and they can be effortlessly separated using a tiny magnet or a simple magnetic separator. The adequate cytotoxicity and magnetic characteristics of the antimicrobial sample suggest a promising future for it in biomedical applications.

The importance of delafossite materials can be attributed to their characterization. They can be classified from insulators to conductors according to their conductivity (σ)[1–4]. For most Cu and Ag-based compounds, the delafossite can be classified as a semiconductor (SC). Pt and Pd-based alloys have good metallic properties[5]. Furthermore, due to its good electric and optical properties, it is classified as a transparent conducting oxide (TCO)[6–8]. The delafossite structure with a general formula contains two cations with different oxidation states (+1 and +3), which provide different sites for further reaction.

Cu, Pt, Pd, or Ag are examples of typical A cations. The B cation is found in distorted edge-shared BO_6 octahedra (B) and has a +3 oxidation state. The cations in the B site can either be p-block metals like In, Ga, and Al or transition metal cations like Co, Fe, and Y[9–11]. The delafossite structure consists of two alternating layers: a layer of edge-sharing BO_6 octahedra and a planar layer of A cations in a triangular pattern with respect to the c-axis[12]. Their NPs also have distinctive characteristics, such as a wide range of chemical compositions, a large surface area, and two active sites for doping with various oxidation states[13].

In recent eras, the increase in microorganisms' resistance to antibiotic treatments has become a concern due to its potentially harmful effects on human health. Therefore, it is critical to find non-precious alternatives based on earth-abundant elements for the control of bacterial and fungal proliferation in uncontrolled environments.

Oxides are the most stable and effective inorganic materials for antimicrobial activity (AMA)[14,15]. Cu, Ni, Fe, and Co-based non-noble transition metal oxides have received a great deal of attention to date. However, delafossite oxides have received little research to date, but they show massive promise for discovering new physics governing the interplay of itinerant and correlated electrons in solids[16]. Among various delafossites, $AgCuO_2$

Physics Department, Faculty of Science, Cairo University, Giza, Egypt. ✉email: atawfik@sci.cu.edu.eg

is particularly desirable for scientific research and potential applications. One of the remarkable and alluring features of $AgCuO_2$ is its appropriate antibacterial efficiency.

Various approaches, mainly solid state[17], sol–gel[18], co-precipitation[19], and hydrothermal precursor[20], have been utilized to synthesize delafossites, but to the best of our knowledge, no prior studies have been conducted using the citrate-auto combustion method. Interestingly, the architecture adopted by the various ABO_2 compounds actually depends on the type of cations and the preparation technique. In this regard, the aim of the present work is to synthesize $AgCuO_2$ NPs with an easy and low-cost technique. The specific objective is to investigate the effect of the preparation method on the size, shape, and polytype of $AgCuO_2$ NPs.

The structure and morphology analyses were carried out via X-ray powder diffraction (XRD) and XPS. The morphology of the $AgCuO_2$ was studied using HRTEM, FESEM, and AFM. The magnetic properties of $AgCuO_2$ NPs were studied using VSM. The authors aimed to examine the AMA of the investigated sample.

Experimental techniques

Preparation of $AgCuO_2$ nanoparticles. The sample $AgCuO_2$ was synthesized using the citrate combustion method[21,22]. As shown in Fig. 1, the stoichiometric ratios of high purity Ag (NO_3), Cu $(NO_3)_2 \cdot 3H_2O$, and citric acid were dissolved in distilled water. The synthesized sample was heated at 400 °C for 4 h at a heating/cooling rate of 4 °C/min.

Sample analysis and characterizations. X-ray powder diffraction (XRD) was performed using a Proker D8 advanced X-ray diffractometer with CuK radiation (λ = 1.5418 Å). The morphology of the investigated sample was studied using Field Emission Scanning Electron Microscopy (FESEM), Atomic Force Microscopy (AFM) and High-Resolution Transmission Electron Microscopy (HRTEM). An EDAX Genesis instrument connected to the SEM column was used to conduct energy-dispersive spectroscopy (EDAX) analysis. SEM Model Quanta 250 FEG is attached. The sample's X-ray photoelectron spectra (XPS) were recorded using K-ALPHA (Thermal Fisher Scientific, USA) with monochromatic X-ray Al K-alpha radiation. Using CASAXPS software, all XPS spectral peaks were fitted, and the data analysis included Shirley background subtraction and spectra normalization. The magnetic hysteresis loop was performed utilizing a vibrating sample magnetometer (VSM; EG & G Model No; 1551, USA) with a maximum applied field of 20 kOe at room temperature.

Antimicrobial activity test. A modified Kirby-Bauer disc diffusion method[23] was used to determine the antimicrobial activity (AMA) of the tested sample. The AMA was tested in vitro using nutritional agar medium against gram-positive bacteria such as *Bacillus subtilis* (*B. subtilis*), *Bacillus cereus* (*B. cereus*), *Enterococcus faecalis* (*E. faecalis*), *Staphylococcus aureus* (*S. aureus*), and gram-negative bacteria such as *Candida albicans* (*C. albicans*) *and Aspergillus*. The sterilized media were added to each of the sterilized Petri dishes (20–25 mL), and they were left to harden at 30 °C. A 1.5×10^5 CFU mL^{-1} microbial suspension was created in sterile saline. 100 µL of the tested compound's solution were added to each well, using a micropipette. In order to test for AMA, the samples were incubated at 37 °C for 24 h, it results in the formation of a zone of inhibition in the form of microbial growth retardation. The zones of inhibition in this experiment were measured on a millimeter scale.

Results and discussion

Structural analyses. ABO_2's structure is based on alternate layers of monovalent cations linearly coordinated with oxygen anions and slightly distorted edge-shared BO_6 octahedra. The delafossite-type oxides can crystallize into the rhombohedral system 3R or the hexagonal crystal system 2H, depending on how these layers are arranged. For the 3R polytype and the 2H polytype, the layers in the delafossite structure are oriented along the c-axis in the following sequences: AaBbCcAa and AaBbAa, respectively. Capital and small letters signify

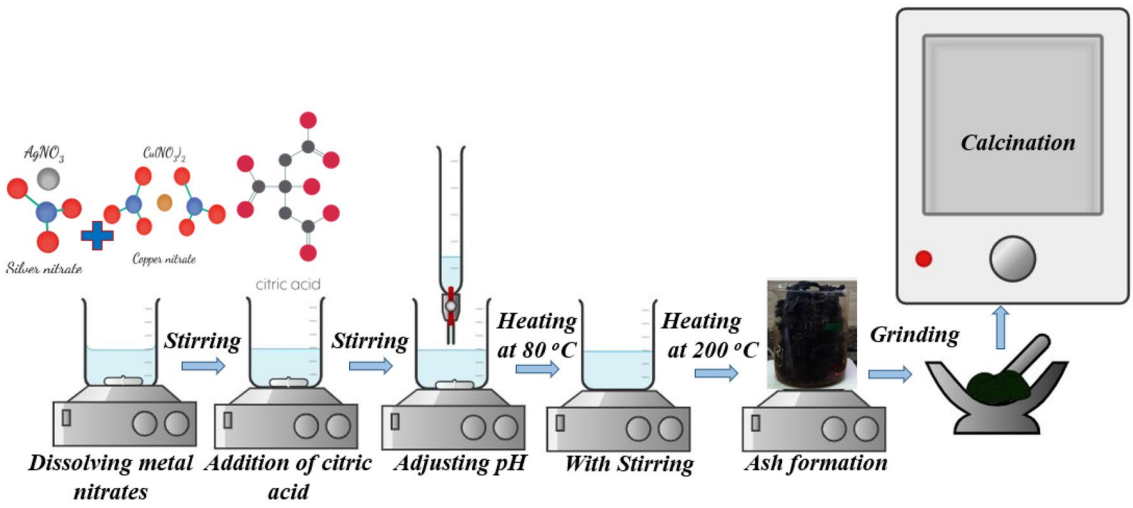

Figure 1. Schematic illustration for the preparation of $AgCuO_2$.

alternate layers of monovalent A^+ cations and $B^{3+}O_6$ octahedrons, respectively. In another way, the identical atom locations are repeated every third layer in a 3R polytype and every second layer in a 2H polytype (Fig. 2c).

Figure 2a shows the XRD diffraction pattern for $AgCuO_2$ NPs. It is clear from the figure that most of the diffraction peaks (006, 101, 012, 310, 104, 009, 018, 0012, and 1010) can be indexed as 3R-$AgCuO_2$ rhombohedral, R-3m, and very little 2H-$AgCuO_2$ (hexagonal, P63/mmc). The diffraction peaks are noticed nearly at the diffraction angles of 38.09°, 44.3° and 64. 9°, and are labelled as (012), (104) and (1010), compared with the Ag XRD pattern. The detected peaks ratified the presence of silver NPs in the investigated system.

These facts can be rationalized by comparing and interpreting the respective crystal structures based on the partial structures of the metal atoms. These are equivalent and fit an ordered variant of $AgIAgIIICuICuIIO_2$ with diverse orientations of the AgO_4 squares and AgO_2 dumbbells in $AgCuO_2$ (see Fig. 6) as relevant from XPS (as will be discussed later).

Furthermore, both crystallite size "D" and lattice strain "ε" have a great effect on peak broadening. As a result, the Williamson-Hall (W–H) method is used for the examination[24]. $AgCuO_2$ has a relatively low ε, as evidenced by the intercept and slope of the (W–H) curve in Fig. 2b, which indicates D to be 36.23 nm and ε to be 1.02910^{-4}.

Figure 3 demonstrates the HRTEM images of the typical nanocrystal. From the figure, it's clear that the NPs are agglomerated. The obtained lattice planes correspond to the crystal plane of $AgCuO_2$. The selected area electron diffraction (SAED) image verifies that the sample is in a crystalline state, which is consistent with the XRD chart.

Figure 4a,b illustrates FESEM photographs of $AgCuO_2$. As can be seen, the $AgCuO_2$ crystals are present as clusters of irregular shape. It is evident that $AgCuO_2$ has a flower-like structure under high magnification, and the granular particles' surfaces are rough and made up of staked NPs. The morphology of the investigated

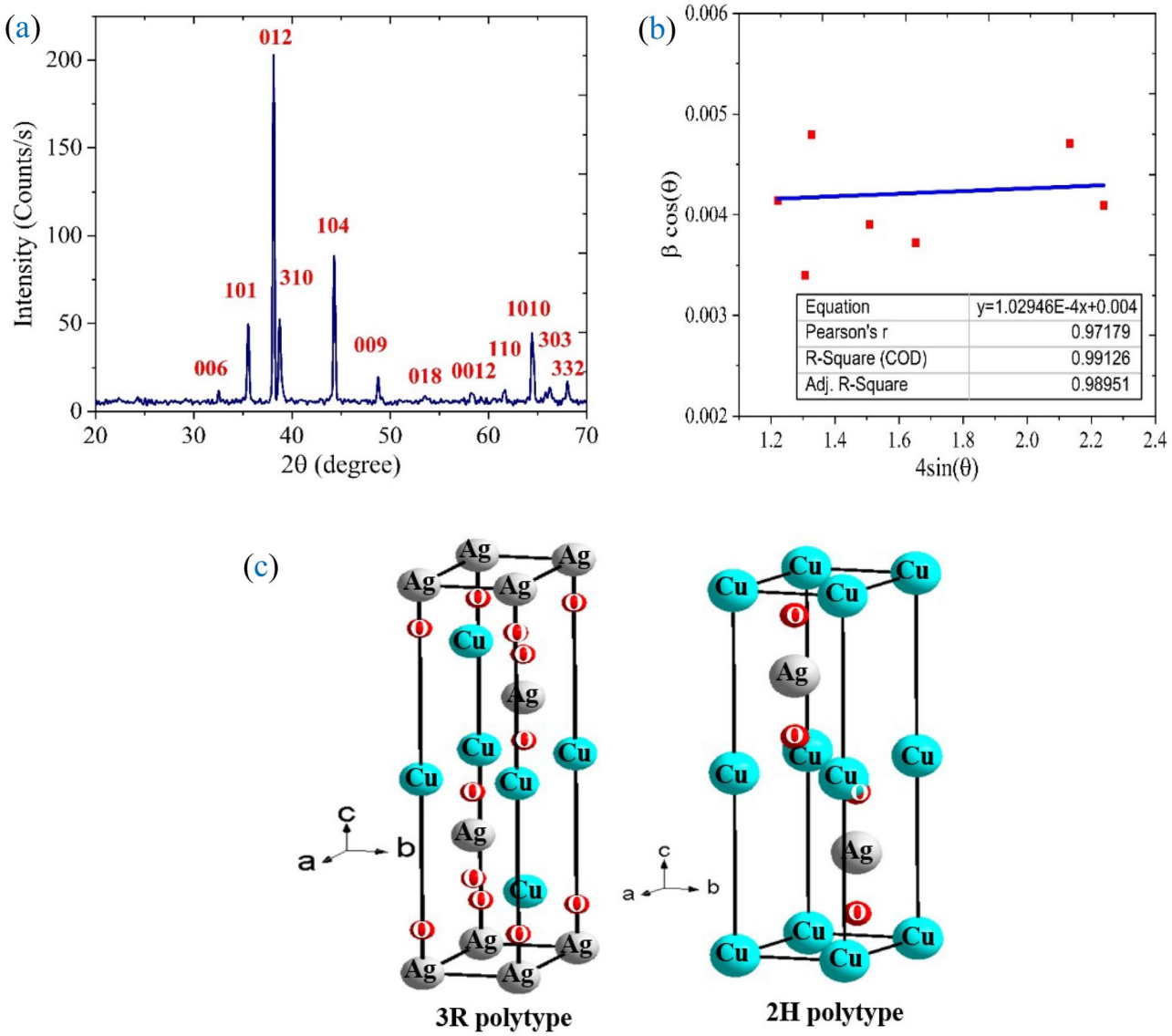

Figure 2. (**a**) XRD pattern of $AgCuO_2$ sample, (**b**) Williamson-Hall plot, and (**c**) 3R and 2H Polytypes of $AgCuO_2$.

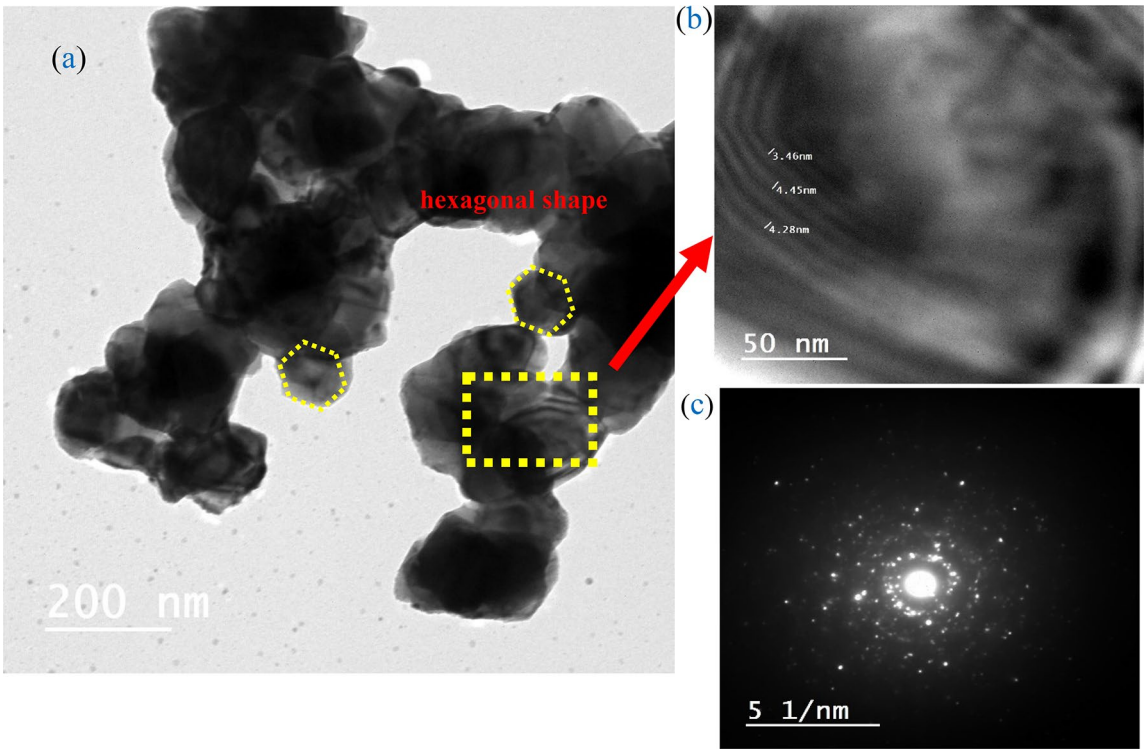

Figure 3. Shows (**a**) the HRTEM image, (**b**) the lattice plane image, and (**c**) the diffraction pattern for the $AgCuO_2$.

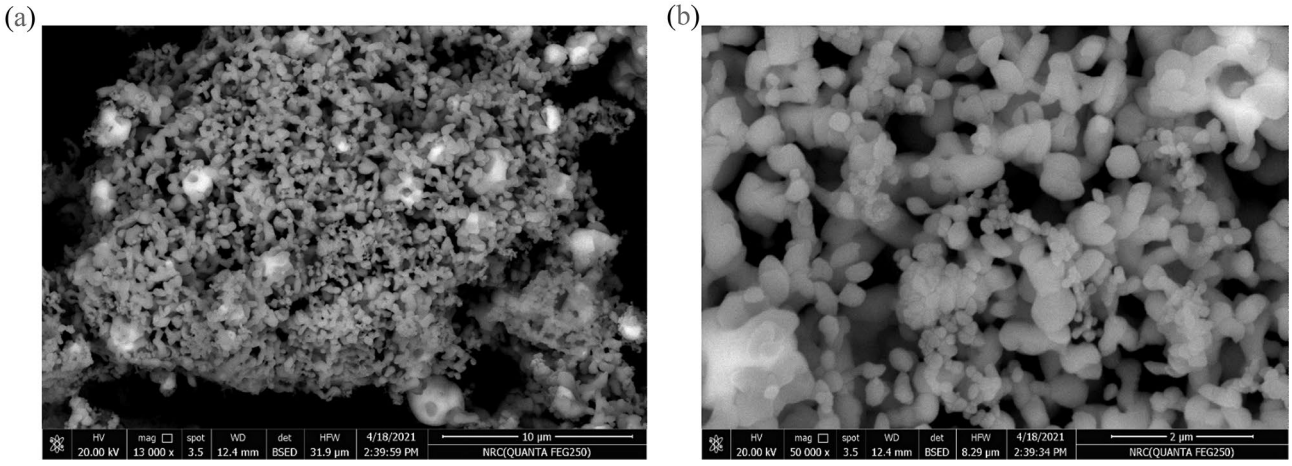

Figure 4. Illustrates the FESEM photographs of $AgCuO_2$ at different magnifications.

NPs accurately depicts the hexagonal platelet-like formations with sharply defined edges, corners, and smooth surfaces.

Figure 5 illustrates the EDAX analysis of $AgCuO_2$. The weight percentage (wt%) and the atomic percentage (at.%) of the elements are revealed in the inset Table. The variation between the theoretical and experimental data can be attributed to oxygen deficiency.

Figure 5b shows the elemental mapping images of Cu, Ag, and O. The images demonstrate the uniform distribution of Ag and Cu and the clustered distribution of Ag, suggesting a homogeneous structure of $AgCuO_2$ NPs.

The XPS survey spectrum of the sample is revealed in Fig. 6a. The existence of Cu, Ag, and O in the synthesized delafossite $AgCuO_2$ NPs with no evidence of any impurity is ratified from the figure. The XPS spectrum of the Ag 3d (Fig. 6b) region is deconvoluted into Ag $3d_{5/2}$ and Ag $3d_{3/2}$ peaks at the binding energies (BE) of 367.9 and 374.08 eV, respectively. The observed doublets are attributed to either a mixture of Ag^{3+} and Ag^{1+} states on the surface of $AgCuO_2$[25,26] or to a single intermediate Ag state classified by multiple splitting[25,26]. The Ag $3d_{5/2}$ spectrum is deconvoluted into two peaks, indicating the presence of Ag(III) and Ag(I)[27]. The width (FWHM) of Ag $3d_{5/2}$ in $AgCuO_2$ is 0.87 eV, which is less than that of Ag(I) oxide (FWHM 1.2 eV). This demonstrates that Ag in $AgCuO_2$ has undergone more than one oxidation state[28].

(a)

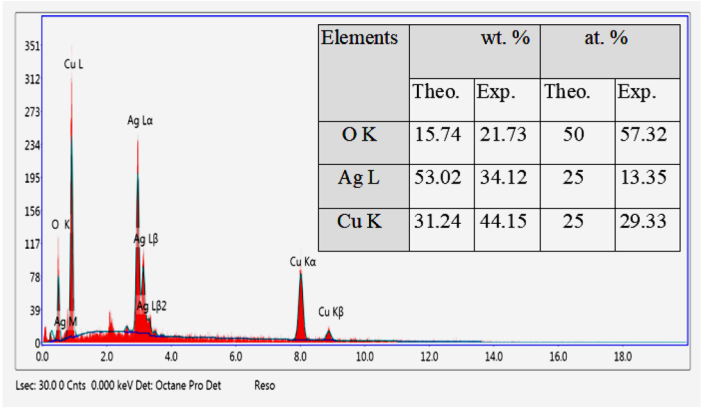

Elements	wt. %		at. %	
	Theo.	Exp.	Theo.	Exp.
O K	15.74	21.73	50	57.32
Ag L	53.02	34.12	25	13.35
Cu K	31.24	44.15	25	29.33

(b)

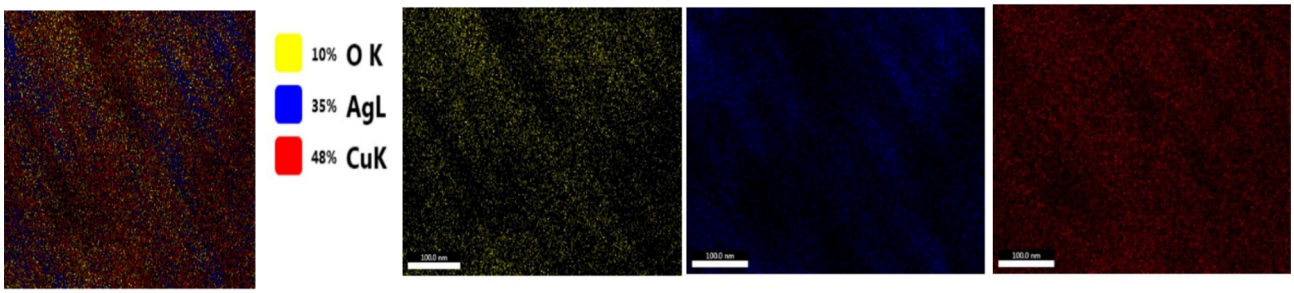

Figure 5. (**a**) EDAX spectra of $AgCuO_2$, and (**b**) elemental mapping images.

At 933.29 and 953.2 eV, respectively, the Cu 2p spectrum (Fig. 6c) can be resolved into $2p_{3/2}$ and $2p_{1/2}$[31].The shoulder peaks located at around 935.05 and 955.27 eV, along with the satellite peaks at 943.68, 941.23, and 961.92 eV, match to Cu $2p_{3/2}$ and Cu $2p_{1/2}$ for Cu^{2+}, which ratify the oxidation of Cu[29].

The valence electron is excited to a higher energy level by an outgoing core electron, which lowers the kinetic energy of the core electron, causing the appearance of the satellite peaks. Since these electrons constitute a component of the overall Cu 2p emission, it is possible to determine the ratio of Cu I: Cu II by looking at the Cu $2p_{3/2}$ peak and associated satellite peak areas.

Using the combined peak areas, it is anticipated that ≈ 52% of the Cu I is converted to Cu II. This estimation implies that every oxygen interstitial is coupled around a copper site, as shown in Fig. 2c.

The O 1s spectrum (Fig. 6d) can be deconvoluted into four component peaks. The oxide species (O^{2-}) are accountable for the observed component peaks at 529.63 and 531.42 eV, where the peroxide species are responsible for the peak component at 532.24 eV[30,31]. At 533.13 eV[35,36], the OH- group can be assigned to the component. One can detect a peak at 532.24 eV corresponding to peroxide species. This suggests that the excess charge on Cu (more than 1+) and Ag (more than 1+) is delocalized onto oxygen as well[28]. Moreover, based on the XPS results, the Ag/Cu ratio amounts to 1:0.99, which agrees well with the EDAX analysis.

AFM investigations are carried out to characterize the surface morphologies of the $AgCuO_2$ as revealed in Fig. 7a,b. The AFM images of the sample reveal grains with a triangular shape, suggesting that the $AgCuO_2$ crystal's facets belong to the rhombohedral lattice. The two directions of the grains are 60° out of phase with one another.

Additionally, the line profiles of the chosen area demonstrate the change in the depth and diameter of the craters on the surface, as shown in Fig. 7c.

The roughness root-mean-square (RMS) value is 15.9 nm. The high RMS value can be attributed to the decrease in surface energy. As a result, the evolution of surface morphology follows the evolution of surface energy in a dominant fashion. The surface particles would not be spread uniformly because atoms tend to gravitate toward sites with higher energies[32–35].

The distributed spiks are evaluated by roughness kurtosis (Rku). The roughness kurtosis has a value of 2.65 (< 3), indicating that the prepared sample is classified as bumpy surface[36].

Magnetic measurements. Figure 8 shows how the magnetization (M) depends on the applied magnetic field for $AgCuO_2$. The data indicate the superparamagnetic behavior of the sample. However, the super-paramagnetic NPs exhibit a nonlinear 'M' plot with nearly no hysteresis or coercive field (Hc)[37]. This is in agreement with the super-magnetic behavior of nanocrystalline delafossite described by Nabiyouni et al.[38]. The magnetic parameters of the testified sample are 32.5×10^{-3} emu/g, 444.93×10^{-6} emu/g, and 41.547 Oe for the saturation magnetization (M_s), retentivity (M_r) and coercivity (H_c) respectively.

The copper atom in the delafossite structure has two O_2 atoms linearly coordinated to it, generating O–Cu–O structures that are parallel to the c-axis. This structure has the shape of a layered triangular lattice, and the O_2 atoms in the O–Cu–O structure are all proportioned with Ag atoms that are parallel to the ab plane. The weak

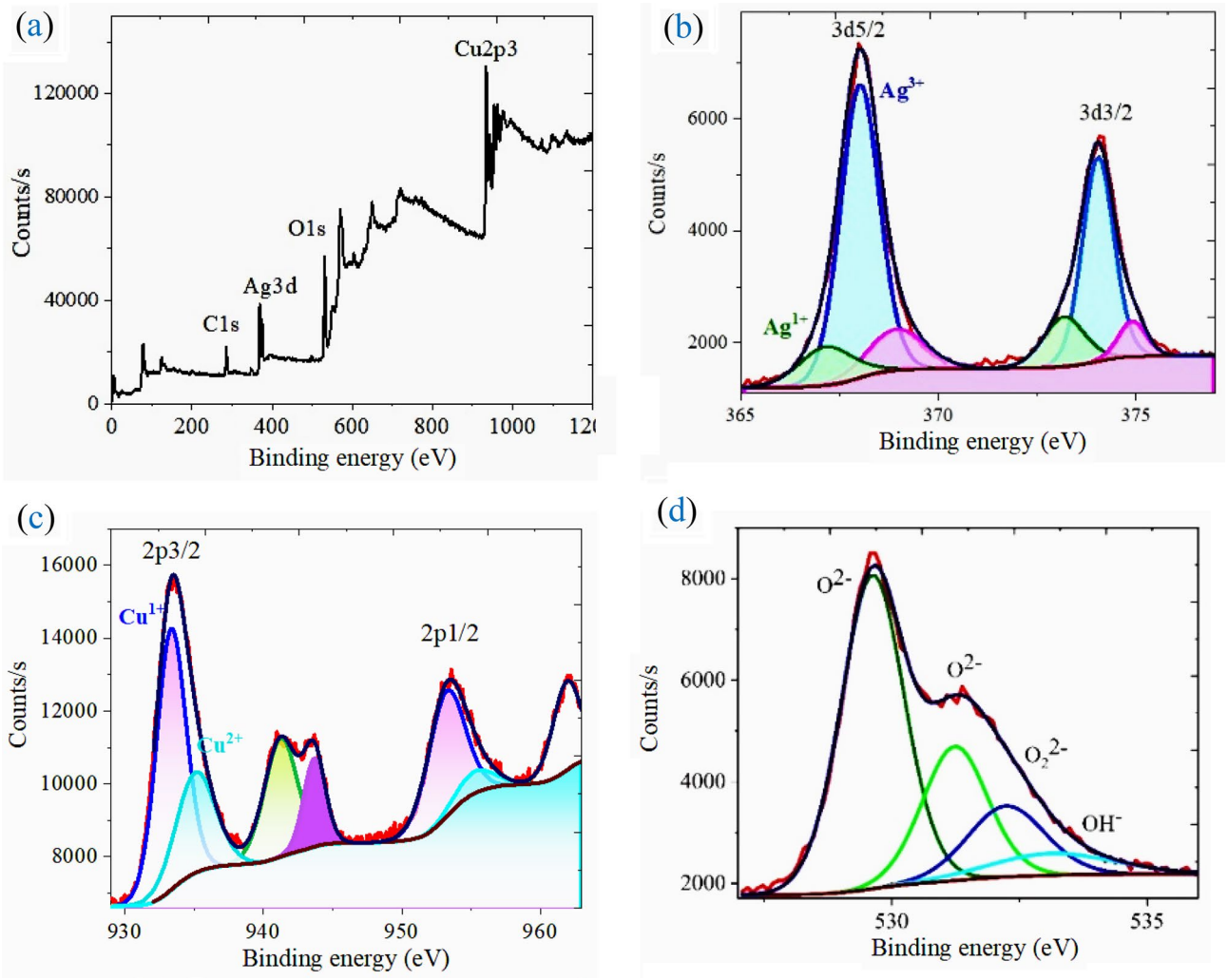

Figure 6. XPS spectra of (**a**) survey, (**b**) Ag 3d, (**c**) Cu2p and (**d**) O1s for the investigated sample.

influence of the Ag–O–Cu interaction is owing to the larger size of Ag 4d orbitals, which increases the distance between magnetic ions and weakens interactions. The lack of hysteresis in $AgCuO_2$ signifies that long-range ordering is not present.

Antimicrobial activity (AMA) of $AgCuO_2$. The as-synthesized $AgCuO_2$ is assessed for in-vitro AMA by the disc diffusion protocol. *Bacillus subtilis (B. subtilis), Bacillus cereus (B. cereus), Enterococcus faecalis (E. faecalis),* and *Staphylococcus aureus (S. aureus)* are used as model gram-positive bacteria in this study. While *Escherichia coli (E. coli), Neisseria gonorrhoeae (N. gonorrhoeae), Pseudomonas aeruginosa (P. aeruginosa),* and *Salmonella typhimrium (S. typhimrium),* are model gram-negative bacterium[39–41]. *Candida albicans (C. albicans),* and *Aspergillus flavus (A. flavus)* are model fungi.

Figure 9a presents the bar values for the achieved zones of inhibition (ZI) with an in-site image for the ZI. According to the results, the $AgCuO_2$ sample has a relatively high ZI against both bacterial strains (+ and −), but no activity against fungus.

$AgCuO_2$ plays a pivotal role that accounts for its effective bactericidal properties. $AgCuO_2$ shows promise in terms of stability, ease of recovery, and low toxicity. Applying $AgCuO_2$ also limits the aggregation and leaching of metallic silver ions. The proven chemical mode of action for inactivating microorganisms is oxidative stress, which is brought on via charge transfer and in-situ reactive oxygen species[42].

The AMA of $AgCuO_2$ is derived from the following three mechanisms. According to the first mechanism, Ag^+ acts at the membrane level because it can pass through the outer membrane and accumulate in the inner membrane, where its adhesion causes damage and destabilization, leading to increased membrane permeability and, ultimately, cell death[43,44].

In the second mechanism, the negative charges on the bacteria's surface, caused by the carboxyl and phosphoric acid groups in the outer membrane, cause Ag^+ to easily concentrate around the active bacterial cells[45]. The thiol (-SH) group of the cysteine chain might interact with the adsorbed Ag^+ by substituting the hydrogen atom to generate –S–Ag, which impairs the affected protein's ability to perform its enzymatic function and prevents the growth of bacterial cells.

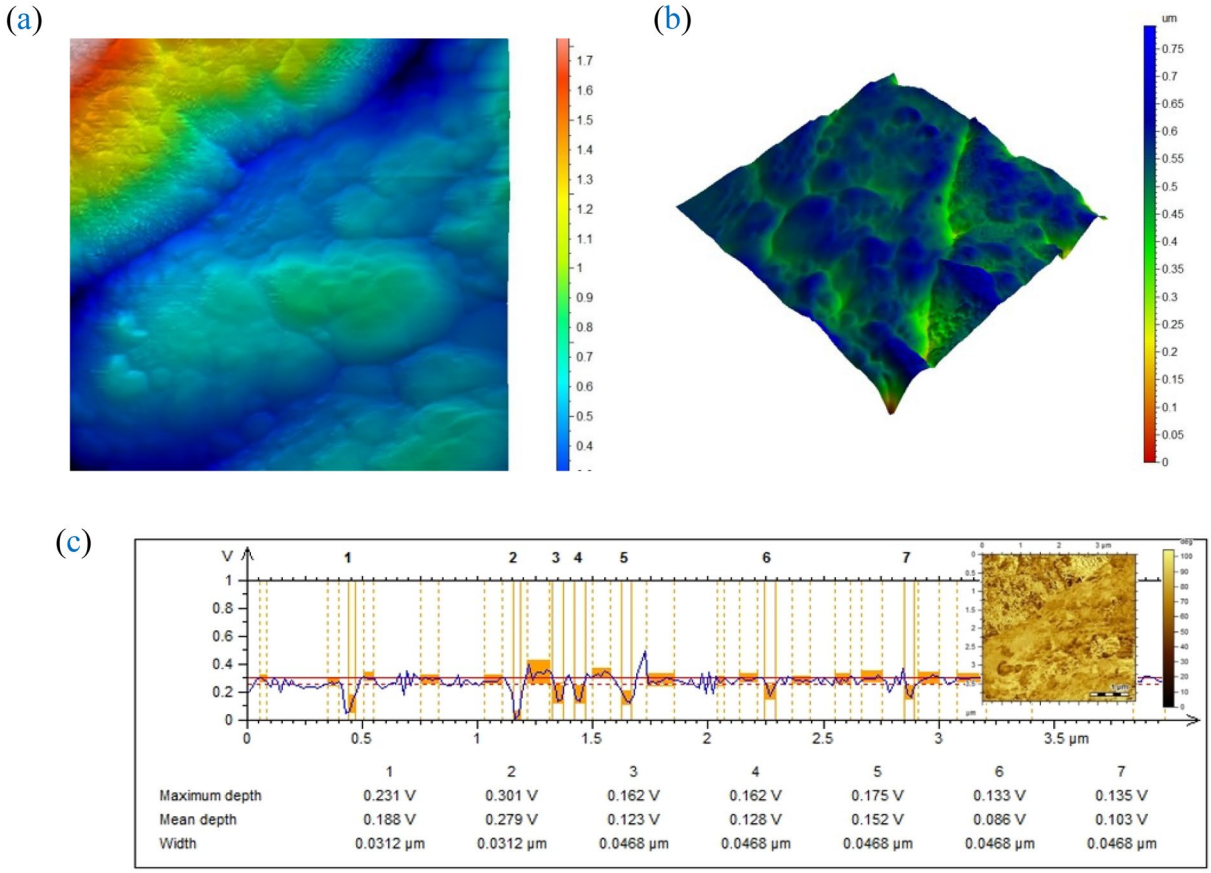

Figure 7. AFM micrographs for the investigated sample.

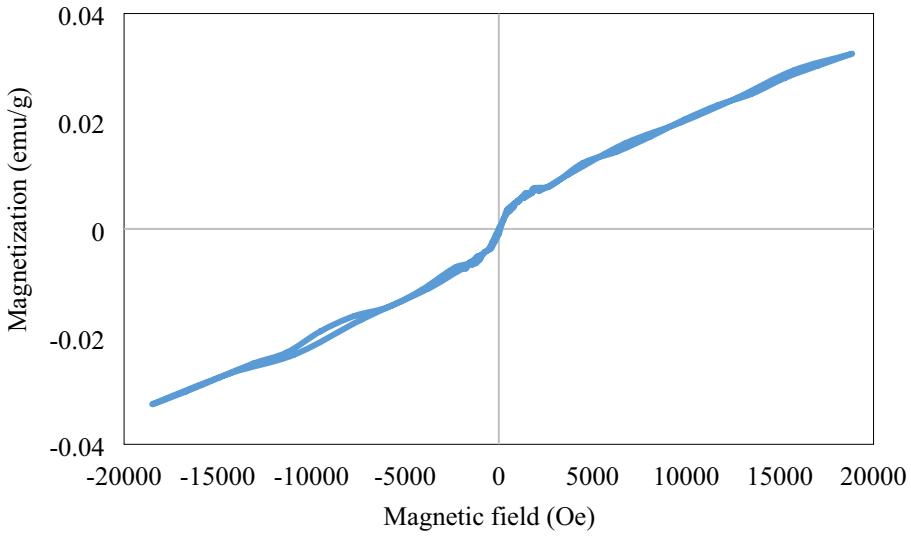

Figure 8. Shows the magnetic hysteresis loop for $AgCuO_2$.

On the other hand, the third mechanism suggested that Ag^+ releases from the NPs and interacts with cellular components, changing metabolic pathways, membranes, and even genetic material. The third mechanism can be proposed to happen concurrently with the other two[46,47].

The percent of viable cells is calculated using the following equation[48]:

$$\text{Dead cell Percent}(\%) = \frac{diameter\ of\ control - diameter\ of\ treated\ sample}{diameter\ of\ control} \times 100 \quad (1)$$

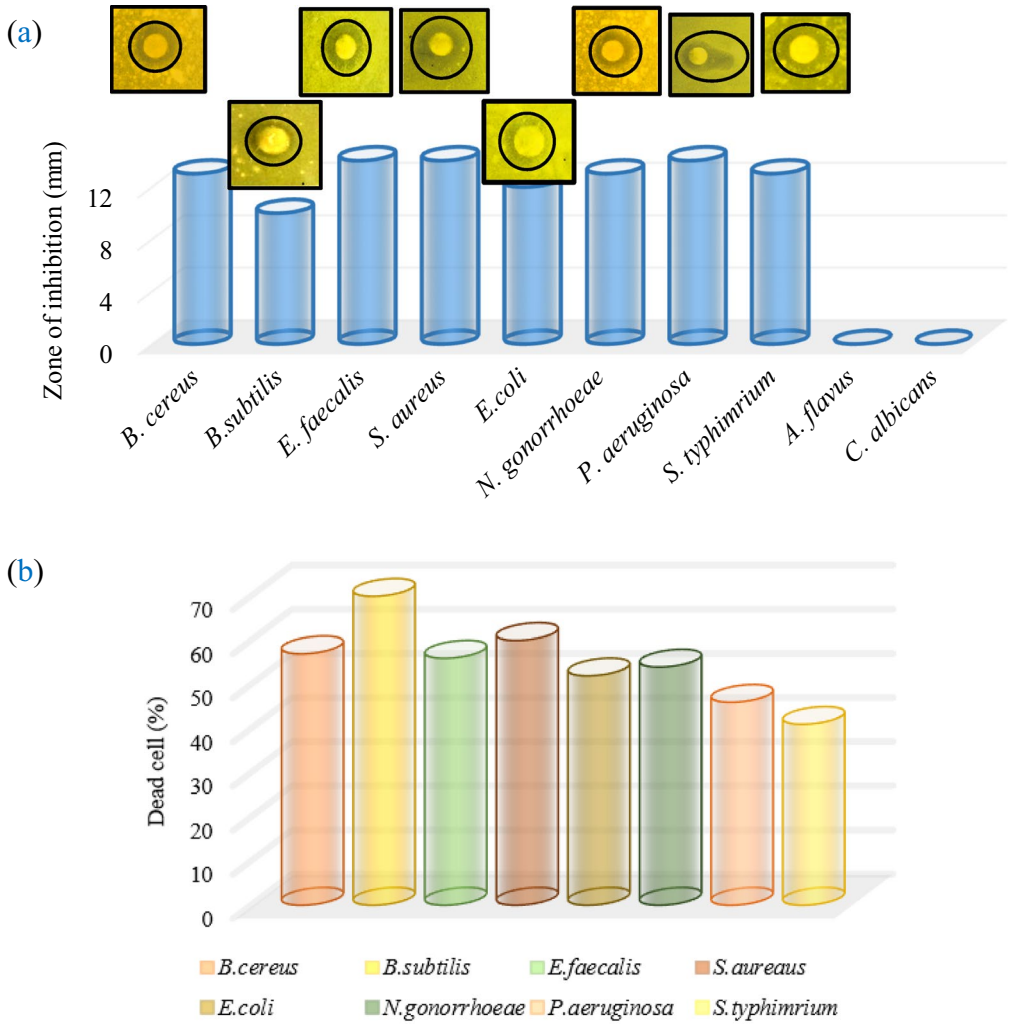

Figure 9. (**a**) The bar values for the achieved zones of inhibition with an in-site image for the inhabitation zone and (**b**) the dead cell %.

The efficiency of the killing of bacteria is presented in Fig. 9b. The maximum efficiency is obtained for *B. subtilis* (70%), while *S. typhimrium* shows the minimum one (41%). The differences in cell wall structure of bacteria play an important role in antimicrobial susceptibility, in this regard, the sample has different activity against Gram-positive and Gram-negative bacteria[49,50].

The multi-oxidation states (Cu (I, II) and Ag (I, III)), and the presence of ROS as relevant from XPS results, besides the nanometric-size, assure the antimicrobial activity of the prepared sample.

Finally, one can conclude that the excellent bactericidal performance of $AgCuO_2$ has been revealed. Thus, it can be used in biomedical and wastewater disinfection applications. Further analysis to confirm the efficiency of $AgCuO_2$ will be performed using other experiments in the future.

Conclusion

The $AgCuO_2$ NPs were successfully synthesized via an easy, low-cost technique. The size and shape of $AgCuO_2$ NPs, along with their structural polytypes of 2H (hexagonal) or 3R (rhombohedral), are dependent on the preparation conditions. The crystallite size (D) and the ε are found to be 36.23 nm and 1.02946×10^{-4} respectively, demonstrating a comparatively low lattice strain in $AgCuO_2$. The hexagonal platelet-like structures with clearly defined edges, corners, and smooth surfaces are well represented by the morphology of the produced particles. The magnetic parameters are recognized, and the superparamagnetic property is achieved at room temperature. $AgCuO_2$, which combines magnetic and highly AMA properties, provides easier separation and high efficiency. As a result, the mineral $CuAgO_2$ is used in medicine as a novel antimicrobial substance.

Data availability

The authors declare that all the data supporting the findings of this study are available in the Crystallography Open Database (COD) repository [entries; 3000419 and 3000420].

Received: 17 October 2022; Accepted: 20 February 2023
Published online: 23 February 2023

References

1. Dordor, P. *et al.* Crystal growth and electrical properties of $CuFeO_2$ single crystals. *J. Solid State Chem.* **75**, 105–112 (1988).
2. Marquardt, M. A., Ashmore, N. A. & Cann, D. P. Crystal chemistry and electrical properties of the delafossite structure. *Thin Solid Films* **496**, 146–156 (2006).
3. Kawazoe, H. *et al.* P-type electrical conduction in transparent thin films of $CuAlO_2$. *Nature* **389**, 939–942 (1997).
4. Garg, A. B. & Rao, R. Copper delafossites under high pressure—A brief review of XRD and Raman spectroscopic studies. *Crystals* https://doi.org/10.3390/cryst8060255 (2018).
5. Mackenzie, A. P. The properties of ultrapure delafossite metals. *Rep. Prog. Phys.* **80**, 32501 (2017).
6. Banerjee, A. N. & Chattopadhyay, K. K. Recent developments in the emerging field of crystalline p-type transparent conducting oxide thin films. *Prog. Cryst. Growth Charact. Mater.* **50**, 52–105 (2005).
7. Walsh, A., Da Silva, J. L. F. & Wei, S.-H. Multi-component transparent conducting oxides: Progress in materials modelling. *J. Phys. Condens. Matter* **23**, 334210 (2011).
8. Zhang, K. H. L., Xi, K., Blamire, M. G. & Egdell, R. G. *P*-type transparent conducting oxides. *J. Phys. Condens. Matter* **28**, 383002 (2016).
9. Esthan, C. *et al.* Transparent heterojunctions of Cu-based delafossites n-$CuInO_2$/p-$CuGaO_2$ by reactive evaporation method for transparent electronic applications. *Vacuum* **197**, 110808 (2022).
10. Lockman, Z., Lin, L. P., Yew, C. K. & Hutagalung, S. D. Rapid formation of transparent $CuAlO_2$ thin film by thermal annealing of Cu on Al_2O_3. *Sol. Energy Mater. Sol. Cells* **93**, 1383–1387 (2009).
11. Keerthi, K., Rahman, H., Jacob, R. & Philip, R. R. Electrical conductivity tuning in p-type transparent conducting $AgGaO_2$ and in quaternary $AgInGaO_2$ thin films. *Mater. Chem. Phys.* **242**, 122506 (2020).
12. Kumar, S. & Gupta, H. C. First principles study of structural, bonding and vibrational properties of $PtCoO_2$, $PdCoO_2$ and $PdRhO_2$ metallic delafossites. *J. Phys. Chem. Solids* **74**, 305–310 (2013).
13. Abdelhamid, H. N. Delafossite nanoparticle as new functional materials: Advances in energy, nanomedicine and environmental applications. *Mater. Sci. Forum* **832**, 28–53 (2015).
14. Abebe, B., Zereffa, E. A., Tadesse, A. & Murthy, H. C. A. A review on enhancing the antibacterial activity of ZnO: Mechanisms and microscopic investigation. *Nanoscale Res. Lett.* **15**, 190 (2020).
15. Ateia, E. E., Hussein, B., Singh, C. & Arman, M. M. Multiferroic properties of $GdFe_{0.9}M_{0.1}O_3$ (M = Ag^{1+}, Co^{2+} and Cr^{3+}) nanoparticles and evaluation of their antibacterial activity. *Eur. Phys. J. Plus* **137**, 443 (2022).
16. Durá, O. J. *et al.* Transport, electronic, and structural properties of nanocrystalline $CuAlO_2$ delafossites. *Phys. Rev. B* **83**, 45202 (2011).
17. Pokhriyal, P. *et al.* Possibility of relaxor-type ferroelectricity in delafossite $CuCrO_2$ near room temperature. *Solid State Sci.* **112**, 106509 (2021).
18. Kongkaew, T., Sinsarp, A., Osotchan, T., Limphirat, W. & Subannajui, K. Magnetic properties and chemical state of nickel doped Cu FeO_2 delafossite oxide powders prepared by sol-gel method. *Mater. Today Proc.* **5**, 10932–10939 (2018).
19. Saib, F. *et al.* Photo-electrochemical properties of p-type $AgCoO_2$ prepared by low temperature method. *Mater. Sci. Semicond. Process.* **91**, 174–180 (2019).
20. Lee, E.-H., Kim, E.-B., Akhtar, M. S. & Ameen, S. Delafossite $CuCrO_2$ nanoparticles as possible electrode material for electrochemical supercapacitor. *Ceram. Int.* **48**, 16667–16676 (2022).
21. Ateia, E. E., Allah, A. A. & Ramadan, R. Impact of GO on non-stoichiometric $Mg_{0.85}K_{0.3}Fe_2O_4$ ferrite nanoparticles. *J. Supercond. Nov. Magn.* https://doi.org/10.1007/s10948-022-06327-0 (2022).
22. Ateia, E. E., Elsayed, K. & Ramadan, R. Tuning the properties of Ba-M hexaferrite $BaFe_{11.5}Co_{0.5}O_{19}$: A road towards diverse applications. *J. Inorg. Organomet. Polym. Mater.* https://doi.org/10.1007/s10904-022-02341-w (2022).
23. Bauer, A. W., Kirby, W. M. M., Sherris, J. C., Turck, A. M. & Graevenitz, A. Von. 40 microbiology: A centenary perspective 1966 antibiotic susceptibility testing by a standardized single disk method. *Am. J. Clin. Pathol.* **45**, 493–496 (1978).
24. Saeid, Y. A. & Ateia, E. E. Efficient removal of Pb (II) from water solution using $CaFe_{2-x-y}Gd_xSm_yO_4$ ferrite nanoparticles. *Appl. Phys. A* **128**, 583 (2022).
25. Muñoz-Rojas, D. *et al.* High conductivity in hydrothermally grown $AgCuO_2$ single crystals verified using focused-ion-beam-deposited nanocontacts. *Inorg. Chem.* **49**, 10977–10983 (2010).
26. Muñoz-Rojas, D., Subías, G., Fraxedas, J., Gómez-Romero, P. & Casañ-Pastor, N. Electronic structure of $Ag_2Cu_2O_4$. Evidence of oxidized silver and copper and internal charge delocalization. *J. Phys. Chem. B* **109**, 6193–6203 (2005).
27. Lu, Q., Lu, K., Zhang, L., Gong, J. & Liu, R. Electrodeposition of $AgCuO_2$ nanoplates. *J. Electrochem. Soc.* **164**, D130–D134 (2017).
28. Padmavathy, N., Vijayaraghavan, R. & Kulkarni, G. U. Solution based rapid synthesis of $AgCuO_2$ at room temperature. *RSC Adv.* **4**, 62746–62750 (2014).
29. Gao, Y. *et al.* Three-dimensional porous Cu@Cu_2O aerogels for direct voltammetric sensing of glucose. *Microchim. Acta* **186**, 192 (2019).
30. Ateia, E. E., Al-Hamzi, A. & Hussein, B. Synthesis and characterization of non-stoichiometric cobalt nanoferrites for multifunctional applications. *J. Mater. Sci. Mater. Electron.* https://doi.org/10.1007/s10854-022-08876-5 (2022).
31. Ateia, E. E., Hussien, S. & Mohamed, A. T. Tuning the structural and magnetic properties of the stuffed framework structures $MeFe_2O_4$ (Me = Ni, Ca, and Sr). *J. Inorg. Organomet. Polym. Mater.* https://doi.org/10.1007/s10904-022-02497-5 (2022).
32. Yao, Z., Wang, C., Li, Y., Kim, H.-K. & Kim, N.-Y. Effects of starting powder and thermal treatment on the aerosol deposited $BaTiO_3$ thin films toward less leakage currents. *Nanoscale Res. Lett.* **9**, 435 (2014).
33. Mine, T. *et al.* Control of carrier concentration and surface flattening of $CuGaO_2$ epitaxial films for a p-channel transparent transistor. *Thin Solid Films* **516**, 5790–5794 (2008).
34. Khojier, K. & Behju, A. Annealing temperature effect on nanostructure and phase transition of copper oxide thin films. *Int. J. Nano Dimens.* **2**, 185–190 (2012).
35. Yu, R.-S. & Hu, D.-H. Formation and characterization of p-type semiconductor $CuCrO_2$ thin films prepared by a sol–gel method. *Ceram. Int.* **41**, 9383–9391 (2015).
36. Ateia, E. E., Mohamed, A. T. & Morsy, M. 5—Functionalized multimetal oxide–carbon nanotube-based nanocomposites and their properties. In *Metal Oxides* (eds Chaudhry, M. A. *et al.*) 103–130 (Elsevier, 2022). https://doi.org/10.1016/B978-0-12-822694-0.00010-7.
37. Ferguson, R. M., Minard, K. R. & Krishnan, K. M. Optimization of nanoparticle core size for magnetic particle imaging. *J. Magn. Magn. Mater.* **321**, 1548–1551 (2009).
38. Nabiyouni, G., Fesharaki, M. J., Mozafari, M. & Amighian, J. Characterization and magnetic properties of nickel ferrite nanoparticles prepared by ball milling technique. *Chin. Phys. Lett.* **27**, 126401 (2010).
39. Aljohny, B. O., Rauf, A., Anwar, Y., Naz, S. & Wadood, A. Antibacterial, antifungal, antioxidant, and docking studies of potential dinaphthodiospyrols from *Diospyros lotus* Linn roots. *ACS Omega* **6**, 5878–5885 (2021).

40. Yang, Y.-Y. *et al.* Fabrication of visible-light-driven silver iodide modified iodine-deficient bismuth oxyiodides Z-scheme heterojunctions with enhanced photocatalytic activity for *Escherichia coli* inactivation and tetracycline degradation. *J. Colloid Interface Sci.* **533**, 636–648 (2019).
41. Yang, Y.-Y. *et al.* Dual-channel charges transfer strategy with synergistic effect of Z-scheme heterojunction and LSPR effect for enhanced quasi-full-spectrum photocatalytic bacterial inactivation: new insight into interfacial charge transfer and molecular oxygen activation. *Appl. Catal. B Environ.* **264**, 118465 (2020).
42. Yashas, S. R. *et al.* Designing bi-functional silver delafossite bridged graphene oxide interfaces: Insights into synthesis, characterization, photocatalysis and bactericidal efficiency. *Chem. Eng. J.* **426**, 131729 (2021).
43. Ivask, A. *et al.* Toxicity mechanisms in *Escherichia coli* vary for silver nanoparticles and differ from ionic silver. *ACS Nano* **8**, 374–386 (2014).
44. Seong, M. & Lee, D. G. Silver nanoparticles against *Salmonella enterica* serotype typhimurium: Role of inner membrane dysfunction. *Curr. Microbiol.* **74**, 661–670 (2017).
45. Li, M. *et al.* Synergistic bactericidal activity of Ag-TiO_2 nanoparticles in both light and dark conditions. *Environ. Sci. Technol.* **45**, 8989–8995 (2011).
46. Li, W.-R. *et al.* Antibacterial activity and mechanism of silver nanoparticles on *Escherichia coli*. *Appl. Microbiol. Biotechnol.* **85**, 1115–1122 (2010).
47. Agnihotri, S., Mukherji, S. & Mukherji, S. Size-controlled silver nanoparticles synthesized over the range 5–100 nm using the same protocol and their antibacterial efficacy. *RSC Adv.* **4**, 3974–3983 (2014).
48. Ahmad, N. *et al.* Polyaniline based hybrid bionanocomposites with enhanced visible light photocatalytic activity and antifungal activity. *J. Environ. Chem. Eng.* **7**, 102804 (2019).
49. Chidurala, S. C., Kalagadda, V. R. & Tambur, P. Antimicrobial activity of pure Cu nano particles synthesized by surfactant varied chemical reduction method. *Environ. Nanotechnol. Monit. Manag.* **6**, 88–94 (2016).
50. Limaye, M. V., Pramanik, M., Singh, S. B., Paik, G. R. & Singh, P. Application of delafossite AgFeO2 nanoparticles as SERS substrate and antimicrobial agent. *ChemistrySelect* **6**, 2678–2686 (2021).

Author contributions

E.E.A.: conceptualization, investigation, curation, validation and visualization, review and editing. M.M.A.: investigation, methodology, data collection, original drafting, review and editing. A.T.M.: material preparation, data collection and analysis, methodology, validation and visualization, original drafting, review and editing. All authors read and approved the final manuscript.

Funding

Open access funding provided by The Science, Technology & Innovation Funding Authority (STDF) in cooperation with The Egyptian Knowledge Bank (EKB). Funding was provided by Cairo University.

Competing interests

The authors declare no competing interests.

Additional information

Correspondence and requests for materials should be addressed to A.T.M.

Reprints and permissions information is available at www.nature.com/reprints.

Publisher's note Springer Nature remains neutral with regard to jurisdictional claims in published maps and institutional affiliations.